*J. Fluid Mech.* (1993), *vol.* 249, *pp.* 161–183



# Turbulence structure and mass transfer across a sheared air–water interface in wind-driven turbulence

By SATORU KOMORI, RYUICHI NAGAOSA AND YASUHIRO MURAKAMI

Department of Chemical Engineering, Kyushu University, Hakozaki, Fukuoka 812, Japan

(Received 21 October 1991 and in revised form 27 October 1992)

The mass transfer mechanism across a sheared air–water interface without bubble entrainment due to wave breaking was experimentally investigated in terms of the turbulence structure of the organized motions in the interfacial region in a wind-wave tank. The transfer velocity of the carbon dioxide ($CO_2$) on the water side was measured through reaeration experiments of $CO_2$, and the fluid velocities in the air and water flows were measured using both a hot-wire anemometer and a laser-Doppler velocimeter. The results show that the mass transfer across a sheared air–water interface is more intensively promoted in wind shear, compared to an unsheared interface. However, the effect of the wind shear on the mass transfer tends to saturate in the high-shear region in the present wind-wave tank, where the increasing rate of mass transfer velocity with the wind shear decreases rapidly. The effect of the wind shear on the mass transfer can be well explained on the basis of the turbulence structure near the air–water interface. That is, surface-renewal eddies are induced on the water side through the high wind shear on the air–water interface by the strong organized motion generated in the air flow above the interface, and the renewal eddies control the mass transfer across a sheared interface. The mass transfer velocity is correlated with the frequency of the appearance of the surface-renewal eddies, as it is in open-channel flows with unsheared interfaces, and it increases approximately in proportion to the root of the surface-renewal frequency. The surface-renewal frequency increases with increasing the wind shear, but for high shear the rate of increase slows. This results in the saturated effect of the wind shear on the mass transfer in the high-shear region in the present wind-wave tank. The mass transfer velocity can be well estimated by the surface-renewal eddy-cell model based on the concept of the time fraction when the surface renewal occurs.

## 1. Introduction

Turbulent mass transfer across wavy gas–liquid interfaces sheared by turbulent gas streams is used as a separation technology in many industrial processes, including gas absorption, evaporation and condensation, and it often occurs in geophysical flows. It is, therefore, of great practical interest to investigate the mass transfer mechanism across such an interface both in designing and controlling industrial equipments with gas–liquid interfaces and in discussing geophysical problems. Recently the accurate estimation of the mass transfer rate has attracted special interest in the global-warming problem related to the exchange of carbon dioxide ($CO_2$) between air and sea.

Usually the resistance on the liquid side dominates the mass transfer across a gas–liquid interface and therefore the mass transfer mechanism has to be clarified in relation to the turbulence structure on the liquid side. However, in wind-driven turbulence with a sheared interface, discussion of the turbulence structure on the liquid side should not be separated from the turbulent motions on the gas side which induce turbulence on the liquid side. There have been few fluid-mechanical studies that have clarified the mass transfer mechanism across wavy sheared gas–liquid interfaces, including the effect of the interfacial shear on the mass transfer rate.

Most studies previously published in the geophysical area have accumulated measurements of mass transfer velocity (mass transfer coefficient or piston velocity) on the liquid side through laboratory experiments (e.g. Wanninkhof & Bliven 1991; Merlivat & Mémery 1983; Jähne 1980; Jähne, Munnich & Siegenthaler 1979; Broecker, Petermann & Siems 1978; Liss 1973) and field observations (e.g. Jähne 1980; Roether & Kromer 1984; Watson, Upstill-Goddard & Liss 1991; Smethie, Takahashi & Chipman 1985), and they then proposed an empirical correlation between the mass transfer velocity and interfacial friction velocity or wind speed. Some studies (e.g. Liss & Merlivat 1986; Jähne *et al.* 1979; Broecker & Peng 1974) have tried to explain the transfer velocity by using a surface-renewal theory, a film theory or other models, without experimental justification, but their explanations have not been successful because of the lack of direct measurements of fluid mechanical properties required in their models.

On the other hand, in the engineering area, a number of studies have measured the mass transfer velocity in thin-film flows and have also discussed the effect of the wind shear on the mass transfer only in terms of the correlation between the transfer velocity and friction velocity (e.g. McCready & Hanratty 1985). However, the turbulence structure is complicated in thin-film flows, since the turbulence is generated by the shear both in the wall region and in the free-surface region. Therefore, it is very difficult to extract only the effect of the wind shear on the mass transfer in such flows. For a non-wavy slip interface where the turbulence is generated both by the wind shear and by the bottom wall in an open-channel flow, Rashidi & Banerjee (1990) and Lam & Banerjee (1992) investigated the turbulence structure both experimentally and numerically, and they found a streaky bursting structure in the sheared slip-interface region which was quite similar to the wall turbulence. Banerjee (1990) estimated the mass transfer coefficient by using the surface-bursting frequency together with a modified surface-renewal model including the idea of turbulent patches. However, they have not yet investigated the turbulence structure and mass transfer at a more wavy gas–liquid interface, where the strong wind-shear generates wind waves and the turbulence is generated over and under the waves by the wind shear only.

The purpose of this study is to experimentally investigate both the turbulent structure near a wavy gas–liquid interface where turbulence is generated only by the wind shear and the effect of the wind shear on the mass transfer across the wavy sheared interface, and then to clarify the relationship between the turbulence structure and mass transfer mechanism. To exclude the effect of the wall turbulence on the gas–liquid interface, the experiments were carried out in a wind-wave tank with a large water depth. The mass transfer velocity on the water side was measured by reaerating $CO_2$ dissolved in the water tank, and the turbulence structure was investigated by measuring both air and water instantaneous velocities above and below the wavy interface.

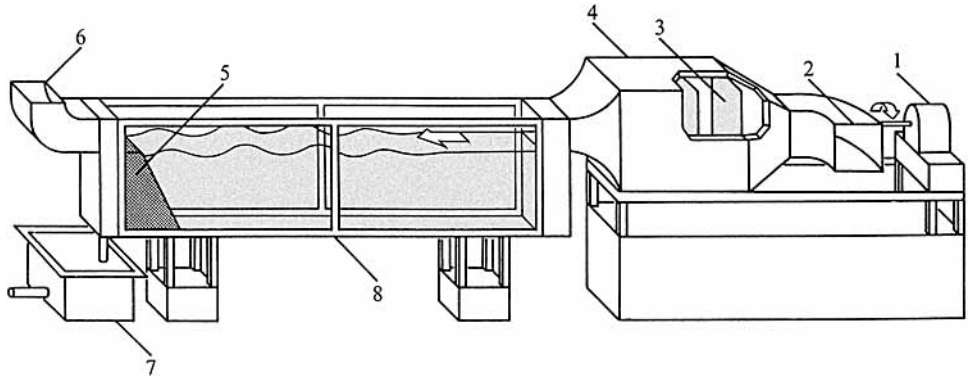


FIGURE 1. Schematic diagram of wind-wave tank: 1, motor; 2, air inlet; 3, screen; 4, wind tunnel; 5, wave absorber; 6, air outlet; 7, drain tank; 8, wind-wave tank.

## 2. Experiments

The apparatus used here was the wind-wave tank shown in figure 1, and it had a glass test section 7 m long, 0.3 m wide and 0.8 m high. The water depth in the tank was 0.5 m, and the vertical height of the air flow above the tank was 0.3 m. Nonlinear three-dimensional waves without bubble entrainment due to intense wave breaking were driven in the water tank by wind with a free-stream velocity in the range $U_\infty = 2.4$–11 m/s, and at the higher velocities the waves were weakly broken. The value of $u_*/c$ was less than 1.05, where $u_*$ is the wind shear (friction velocity) at the interface and $c$ is the phase speed of wind waves. The upper limit of the free-stream velocity was set by the power of the present wind fan. The phase speed $c$, the wave frequency $f_W$, the wave height $h$ and the wavelength $\lambda$ were measured using a high-speed video system (NAC: HSV400), and the statistical characteristics of the waves at $x = 5$ m, together with the averaged values of the measurements of the mass transfer velocity $\overline{k_L}$, are listed in table 1 for several main runs. The measurements were done in the region (fetch) $x = 3$–5 m from the entrance ($x = 0$) of the tank, where typical wind waves were generated.

Instantaneous streamwise and vertical velocities were simultaneously measured at $x = 3$ and 5 m by using a constant-temperature hot-wire anemometer (DANTEC 56C16) with a miniature X-probe (DANTEC 55P61) in the air flow, as shown in figure 2. The velocities in the water flow were measured using a two-colour laser-Doppler velocimeter (DANTEC 55X) with a forward scattering mode. The hot-wire and laser probes were vertically traversed up to just above the crests and below the valleys of the waves, respectively. Unfortunately the velocities in the immediate vicinity of the averaged interface, i.e. in the waves, could not be measured as well as in previous studies (e.g. Cheung & Street 1988), since both hot-wire and laser probes were intersected by the three-dimensional waves. However, the present wave heights were small enough ($h < 0.012$ m) that it was possible to detect the organized motions with scales larger than or comparable to the wave height. The measured velocity signals were transmitted directly into a digital recorder (TEAC DR-1000) and stored on a magnetic tape. The sampling interval and sample size were 0.001 s and 300000, respectively. The digital signals were processed statistically by a digital computer.

In addition to the velocity measurements, the flow visualization was carried out in both the air and water flows. For the air flow, a smoke-wire technique was adopted

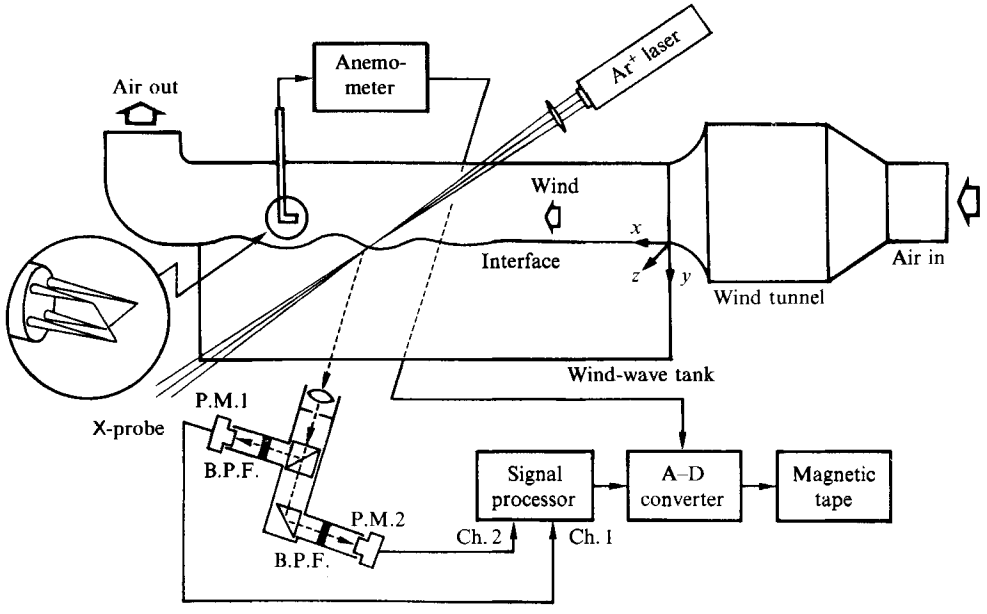


FIGURE 2. Schematic diagram of velocity-measurement system.

| $U_\infty$ (m/s) | $u_*$ (m/s) | $c$ (m/s) | $f_w$ (1/s) | $h$ (m) | $\lambda$ (m) | $\bar{k}_L$ (m/s) |
|---|---|---|---|---|---|---|
| 4.02 | 0.16 | 0.38 | 8.40 | 0.001 | 0.040 | $4.28 \times 10^{-5}$ |
| 4.49 | 0.19 | 0.37 | 8.00 | 0.001 | 0.038 | $6.08 \times 10^{-5}$ |
| 5.15 | 0.23 | 0.41 | 6.45 | 0.002 | 0.057 | $9.17 \times 10^{-5}$ |
| 6.65 | 0.38 | 0.52 | 4.95 | 0.004 | 0.099 | $9.48 \times 10^{-5}$ |
| 8.06 | 0.46 | 0.53 | 4.57 | 0.006 | 0.126 | $9.56 \times 10^{-5}$ |
| 9.60 | 0.60 | 0.63 | 3.62 | 0.010 | 0.171 | $9.45 \times 10^{-5}$ |
| 11.0 | 0.73 | 0.70 | 3.10 | 0.012 | 0.215 | $1.04 \times 10^{-4}$ |

TABLE 1. Statistical characteristics of wind waves at $x = 5$ m and mass transfer velocity $\bar{k}_L$ for the main runs

and the paraffin mist was fed over the waves. In the water flow, sodium fluorescein dye was used, illuminated by a high-power argon-ion laser (LEXCEL model 95-4). The flow patterns of the smoke and dye were viewed from the sidewall of the wind-wave tank and were recorded at intervals of 0.0025 s by using the high-speed video system. Each frame of the recorded pictures was carefully analysed by eye, as objectively as possible.

The mass transfer velocity on the water side, $k_L$, was measured through $CO_2$ reaeration experiments. First, pure $CO_2$ was excessively dissolved into filtered tap water at 20 °C in the water tank, and the water with $CO_2$ was homogeneously mixed in the tank. Then the fan in the wind tunnel was turned on and the mean concentration of $CO_2$ on the air side was measured vertically at $x = 3$ and 5 m by using two sampling tubes connected to $CO_2$ analysers (FUJI ELEC ZFP5), based on infrared spectroscopy with a resolution of 5 p.p.m., as shown in figure 3. The bulk concentration of $CO_2$ on the water side was measured by a sampling tube connected to a total organic carbon meter (SHIMAZU TOC-5000). From these concentration measurements, the reaeration rate from the water into the air was estimated, and then the mass transfer velocity on the water side was calculated from the rate.

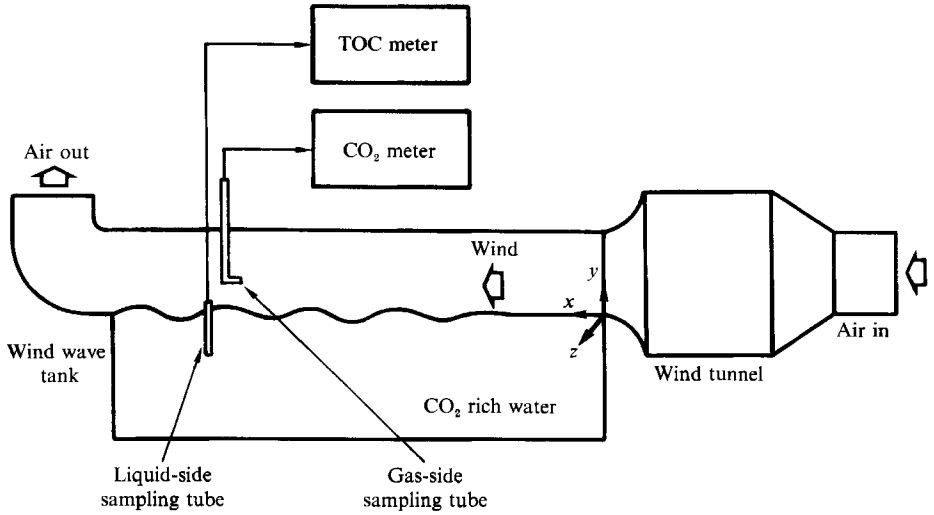


FIGURE 3. Schematic diagram of concentration-measurement system.

## 3. Results and discussion

### 3.1. *Effect of interfacial shear on mass transfer*

To estimate the friction velocity $u_*$ at the air–water interface the mean velocity and the Reynolds stress were measured in the air flow above the interface. Figures 4(*a*) and 4(*b*) show the distributions of the mean velocity $U_G$ and the Reynolds stress $-\overline{u_G v_G}$ against the vertical distance $y$ from the averaged water surface ($y = 0$), respectively. A logarithmic boundary layer was clearly observed in all runs, and the Reynolds stress became almost constant in the logarithmic boundary layer. The constant Reynolds stress based on the air-phase density $-\rho_G \overline{u_G v_G}$ agreed well with the Reynolds stress on the water side $-\rho_L \overline{u_L v_L}$ measured just below the valley of the wave. The distributions of Reynolds stress in the air flow are quite similar to the measurements of Kawamura & Toba (1988), who showed, by using a hot-wire probe moving synchronously with the wave, which enabled velocity in the waves to be measured, that $-\overline{u_G v_G}$ becomes constant up to the averaged water surface ($y = 0$). Thus, the friction velocity $u_*$ on the air side was estimated by applying both the logarithmic law with a von Kármán's constant of 0.4 and the assumption of a constant-flux layer. Figure 5 shows the friction velocities estimated by the two methods against the free-stream velocity $U_\infty$. They agree well, and they are well correlated with the free-stream velocity:

$$u_* = 0.02 U_\infty^{\frac{3}{2}}. \tag{1}$$

This equation is an empirical formula and the constant of 0.02 should have the dimension of $(\mathrm{m/s})^{-\frac{1}{2}}$. The correlation is in quite good agreement with the results of Plant & Write (1977), Hidy & Plate (1966) and others in wind-wave tanks and it is also close to the correlation of $u_* = 0.016 U_\infty^{\frac{3}{2}}$ found by Wanninkhof & Bliven (1991) for well developed waves in a huge wave tank. The results suggest that our wind-wave tank is very similar to wind-wave tanks used in many previous laboratory measurements. The values of $u_*$ estimated by the logarithmic law at $x = 3$ m are also shown on figure 5 by solid circles, and they agree well with the values at $x = 5$ m. Merlivat & Mémery (1983) also confirmed in a wind-wave tank with almost the same dimensions as the present wind-wave tank that a constant-flux boundary layer has

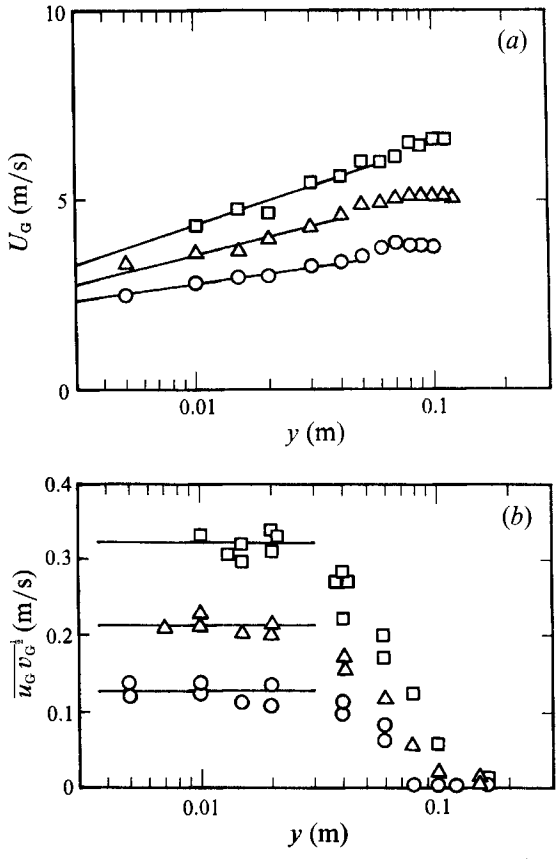


FIGURE 4. Distributions of (*a*) mean velocity and (*b*) Reynolds stress in the air boundary layer: ○, $U_\infty = 3.8$ m/s; △, $U_\infty = 5.1$ m/s, □, $U_\infty = 6.6$ m/s. Lines show the logarithmic boundary layer.

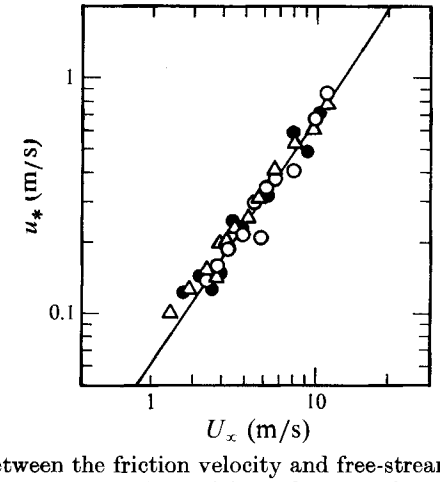


FIGURE 5. Correlation between the friction velocity and free-stream velocity: ○, estimated from the logarithmic law at $x = 5$ m; ●, estimated from the logarithmic law at $x = 3$ m; △, estimated from the assumption of a constant-flux layer. A line shows (1).

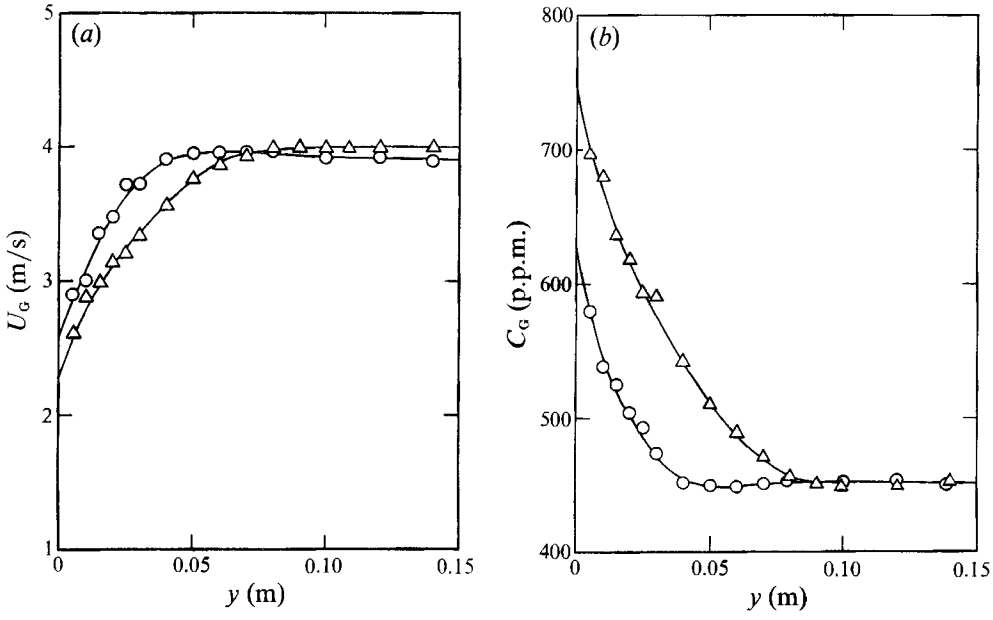


FIGURE 6. Vertical distributions of (*a*) mean velocity and (*b*) mean concentration in the air boundary layer with $U_\infty = 4.0$ m/s: at ○, $x = 3$ m; △, $x = 5$ m. Lines show the best-fitting curves.

developed in their measurement region (fetch) between $x = 3.7$ and 5.7 m. This suggests that in the region $x \geqslant 3$ m constant energy is transferred from the air flow to growing waves and turbulence in the water flow. Furthermore, Plant & Wright (1977) have showed that $u_*$ grows rapidly in the region $x < 1$ m.

Figure 6(*a*, *b*) shows typical profiles of the mean velocity and concentration measured at $x = 3$ and 5 m in the air boundary layer. The velocity profiles show the development of the boundary layer because of wave roughness downstream, and the velocity in the outer layer becomes a little smaller in the downstream region, because of the limited height of the closed duct over the waves. The reaeration rate of $CO_2$ from the water into the air flow was estimated by vertically integrating the product of the mean velocity and concentration, and then subtracting the product at $x = 3$ m from that at $x = 5$ m. The errors in the reaeration rate due to the extrapolation of mean velocity and concentration to the elevation of the averaged interface ($y = 0$) in the waves was negligibly small. Also, the effect of taking the reaeration area to be between $x = 3$ and 5 m on the reaeration rate per unit area was checked by changing both the reaeration area to $x = 4$ and 6 m and the 2 m length of the reaeration area to 1 m in the region $x = 3$–6 m. The results showed that the effects are negligible, and they also suggested that the wave growth rate may be roughly the same throughout the region $3 \leqslant x \leqslant 6$ m.

The mass transfer velocity on the water side, $k_L$, was estimated from the reaeration rate per unit area, $N$, by

$$N = k_L(C_b - C_*), \tag{2}$$

where $C_b$ is the bulk concentration of $CO_2$ on the water side and $C_*$ denotes the equilibrium concentration at 20 °C and 1 atm. The bulk concentration in the water was almost the same between $x = 3$ and 5 m during the experiments, as shown in figure 7, and therefore the average of the values at the two locations was used. As

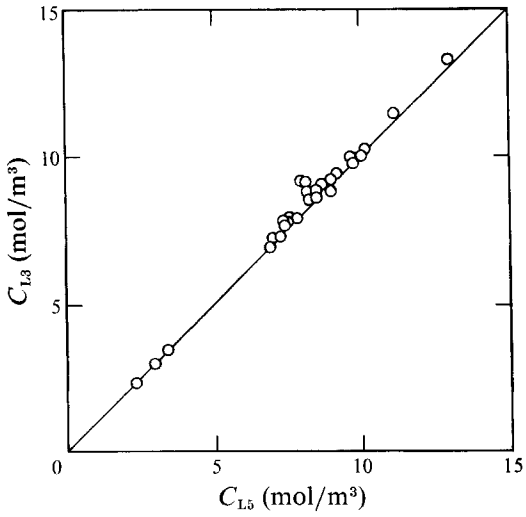


FIGURE 7. Comparison of the bulk concentration of $CO_2$ measured at $x = 3$ m in the water, $C_{L3}$, with that at $x = 5$ m, $C_{L5}$.

long as the bulk concentration of $CO_2$ was maintained higher than 2.5 mol/m$^3$, the concentration variation with time was negligibly small for the measurement period of one run. Also, it was confirmed that the measured values of $k_L$ do not vary over time. The equilibrium concentration was estimated by Henry's law and the partial pressure of $CO_2$ was determined from the concentration of $CO_2$ at the interface, obtained by extrapolating the concentration profile (see figure 6*b*). However, the equilibrium concentration was two orders of magnitude smaller than the bulk concentration and therefore $k_L$ was not affected even when the partial pressure was determined from the $CO_2$ concentration at the outer edge of the air boundary layer (i.e. $CO_2$ concentration in the fresh air). This showed that the mass transfer rate is controlled in the liquid phase.

Figure 8(*a*) shows the variation of the mass transfer velocity on the water side with the friction velocity on the air side. The mass transfer velocity $k_L$ rapidly increases with increasing friction velocity $u_*$ in the region $u_* < 0.25$ m/s, and it reaches about ten times the values measured by Komori, Murakami & Ueda (1989) and Komori, Nagaosa & Murakami (1990) in open-channel flows with unsheared (zero shear) air–water interfaces. This shows that the mass transfer is strongly promoted by the interfacial wind shear. However, the increase in $k_L$ becomes more gentle in the high-shear region $u_* > 0.25$ m/s and $k_L$ tends to approach a constant value. The reason why $k_L$ tends to saturate in the high-shear region will be discussed later. Here it should be noted that the values of $k_L$ in the higher-shear region are very close to the measurements of McCready & Hanratty (1985) in a thin-film flow as shown by the dotted area in the figure. This suggests that the turbulent motions induced by the wind shear control the mass transfer across highly sheared air–water interfaces even in thin-film flows where turbulent motions are produced by both wind shear and wall shear.

In previous work in the geophysical area, a continuous increase of $k_L$ has been assumed even for highly sheared interfaces without bubble entrainment due to intense wave breaking, and all laboratory and field measurements of $k_L$ have been arranged under the preconception of the proportionality between $k_L$ and $u_*$ or $U_\infty$. As shown in figure 8(*b*), most previous measurements in wind-wave tanks and fields

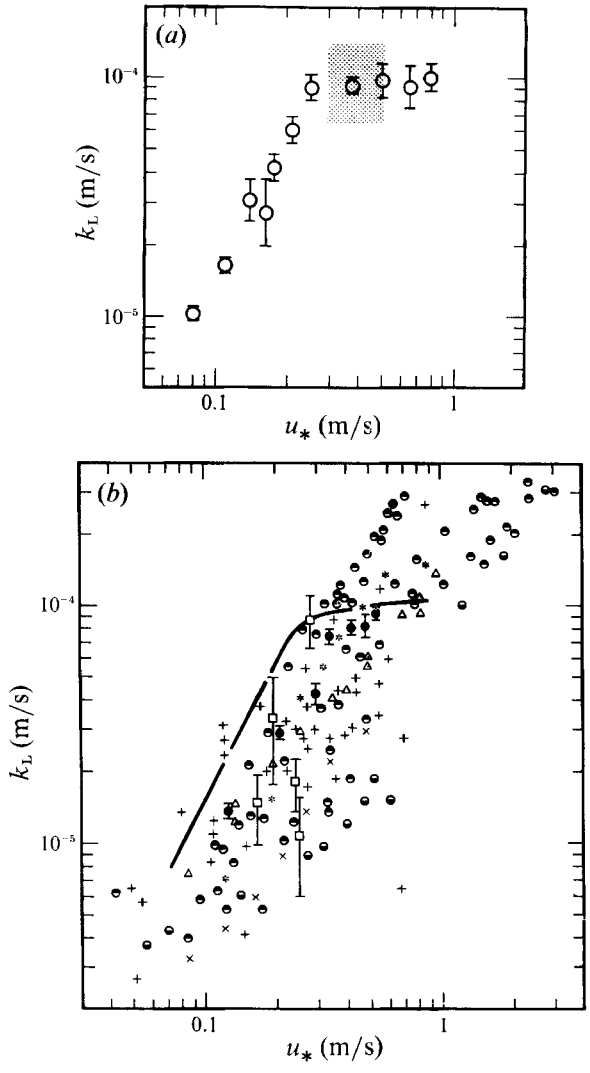


FIGURE 8. Variation of the mass transfer velocity with the friction velocity. (*a*) Present data and a comparison with the measurements in a thin-film flow of McCready & Hanratty (1985). The dotted area indicates the extent of the measurements of McCready & Hanratty (1985). (*b*) Comparisons with the previous measurements in wind-wave tunnels and fields; ●, laboratory data ($N_2O$) of Merlivat & Mémery (1983); ◓, laboratory data ($CO_2$) of Jähne (1980) from Jirka & Brutsaert (1984); ◒, laboratory data ($CO_2$) of Jähne *et al.* (1979); *, laboratory data ($CO_2$) of Broecker *et al.* (1978) from Jähne *et al.* (1979); ×, laboratory data ($O_2$) of Liss (1973) from Jähne *et al.* (1979); △, laboratory data ($SF_6$) of Wanninkhof & Bliven (1991) for the whole tank range; □, field data ($CO_2$) of Roether & Kromer (1978); +, field data ($CO_2$) of Jähne (1980) from Jirka & Brutsaert (1984). Field data are converted from the measurements of $k_L$ for radon by using the surface-renewal concept $k_L \propto$ (molecular diffusivity)$^{\frac{1}{2}}$. The solid line shows a best-fit curve of the present measurements in (*a*).

are very scattered among individual studies, and they seem to show a rough proportionality between $k_L$ and $u_*$. It will, therefore, be interesting to inspect more carefully the previous measurements. We should exclude the field data, because they are not direct measurements; that is, the field data are converted from the measurements of $k_L$ for radon by using the surface-renewal concept of $k_L \propto$ (molecular diffusivity)$^{\frac{1}{2}}$. Also, the field data may include the effect of the con-

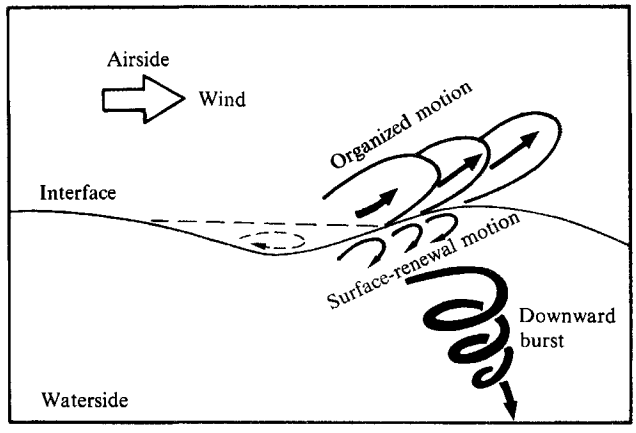


FIGURE 9. Sketch of the organized motions above and below the wave.

tamination in the sea water. The laboratory data of Merlivat & Mémery (1983) and Wanninkhof & Bliven (1991) may be more reliable and they should be carefully inspected. The measurements in fresh water by Merlivat & Mémery (1983) exhibit a very similar trend to the present measurements even in the highly sheared region, but they suddenly jump up in the region $u_* > 0.6$ m/s. This behaviour can also be seen at $u_* > 0.9$ m/s (see figure 6 of Wanninkhof & Bliven 1991). However, Wanninkhof & Bliven (1991) regarded the increase of $k_L$ with $u_*$ as continuous, since data around $u_* = 0.6$ are lacking. In particular, it is interesting that the relationship between the radar backscatter from the disturbances on the wave and the friction velocity (see figures 8 and 9 of Wanninkhof & Bliven 1991) is very similar to the present relationship between the mass transfer velocity and the friction velocity. Furthermore, a few field measurements (e.g. in figure 1 of Watson *et al.* 1991) seem to show a similar trend of $k_L$ to our measurements and suddenly jump in the extremely sheared region $U_\infty > 15$ m/s, though their data are not shown in figure 8(*b*) because they did not measure friction velocity. These results suggest that $k_L$ increases with $u_*$ in the weakly sheared region and its rate of increase becomes small in the highly sheared region. In the extremely sheared region $k_L$ jumps up and, in fact, our quite recent measurements in an amended wind-wave tank with a more powerful wind fan suggest a jump in the region of $u^* > 0.8$ m/s. The criterion for the jump may depend on the rate of the bubble entrainment due to intense wave breaking, as also remarked by Merlivat & Mémery (1983). This suggests that the gas transfer mechanism changes at the shear level near the jump ($u_* \approx 0.8$ m/s): that is, below this level ($u_* < 0.8$ m/s), the mass transfer will be controlled by the surface-renewal eddies appearing in the interfacial region as discussed later, whereas above it ($u_* > 0.8$ m/s) mass transfer will be controlled both by the surface-renewal eddies and dispersed small bubbles (i.e. mass transfer across the interfaces around the bubbles) in the water phase. Therefore, a monotonic proportionality between $k_L$ and $u_*$ would not be expected in the extremely sheared region and there we will have to consider the effects of the complicated mass transfer between the water and bubbles (e.g. Broecker & Siems 1984).

### 3.2. *Turbulence structure near the sheared air–water interface*

Figure 9 shows a sketch of the organized motions above and below the air–water interface, obtained from the high-speed video pictures which were visualized by means of paraffin smoke and laser dye. The organized motion in the air flow above

the interface intermittently appears in front of the wave crest and generates an upward-accelerated bulge of smoke as also shown by Kawamura & Toba (1988). The organized motion in the air flow above the highly sheared wavy interface is generated by the three-dimensional wave. The generation mechanism will be different from the bursting phenomena observed near the smooth rigid wall, since the intermittent organized motion is always observed in front of the wave crest as sketched in figure 9. On the other hand, Rashidi & Banerjee (1990) and Banerjee (1990) have observed streaky structures at the non-wavy gas–liquid interface in a counter-current air–water open-channel flow with high interfacial shear, which are quite similar to those found near the rigid wall, and they suggested that the bursting motions are generated in the interfacial region of the water flow. Furthermore, they estimated a bursting frequency which is proportional to $u_*^2$. The bursting structure may be right for a weakly sheared interface with small wave heights close to a non-wavy interface. However, for a highly sheared interface with comparatively large wave height the turbulence structure rather resembles the structure above a solid wavy wall as shown by dashed lines in figure 9, though neither air separation nor recirculating flow behind the wave crest could be clearly visualized because of the difficulty of the feed of the smoke into the waves. Zilker & Hanratty (1979) have measured the shear stress above a two-dimensional solid wavy wall and have showed that the shear stress becomes a maximum in front of the wavy wall crest where the separated air reattaches. Very recently, the direct numerical simulations by Komori, Nagaosa & Murakami (1993) have also showed that organized motion rather similar to the present motion appears in front of the two-dimensional wavy wall crest where the instantaneous shear stress and pressure are maximum, and the motion is accelerated above the crest in the outward direction. Of course, it should be noted that the present waves are three-dimensional and the flow structure may be a little different from that over a two-dimensional solid wavy wall.

On the water side the surface-renewal motion appears intermittently and frequently, and it renews the free surface like a rolling eddy. The frequency of appearance of the surface-renewal eddies in the high-shear region is far larger than the typical frequency of the waves (see figure 14*b*) and the scale of a surface-renewal eddy is roughly estimated to be 0.05–0.5$\lambda$. Also the surface-renewal motion is observed to be generated below the interface at the same place where the organized motion in the air flow occurs, as sketched in figure 9. This suggests that the surface-renewal motion in the water flow is induced in front of the wave crest by the strong shear due to the organized motion in the air flow. In addition to the surface-renewal motion, strong downward bursts with a large scale are intermittently observed, which spirally intrude into the bulk water as shown in figure 9. A burst is likely to be associated with the wave motion, and their frequency of appearance and scale are roughly equal to the wave frequency and the wavelength. Similar large-scale downward bursts were also observed by Yoshikawa *et al.* (1988). Such bursts may be produced by the drift of three-dimensional waves through a kind of drive mechanism like Langmuir circulation; however, we could not clarify the details of their structure and generation mechanism. Furthermore, we could not investigate whether a downward burst is one of the above surface-renewal motions or not, i.e. we had no information about the relationship between the surface-renewal motion and such bursts. At the present stage, we can only mention that the scale of the surface-renewal motion is rather smaller than that of a strong downward burst which can be clearly visualized, and their frequency of appearance is rather larger.

The organized motion, in particular the surface-renewal motion in the water flow,

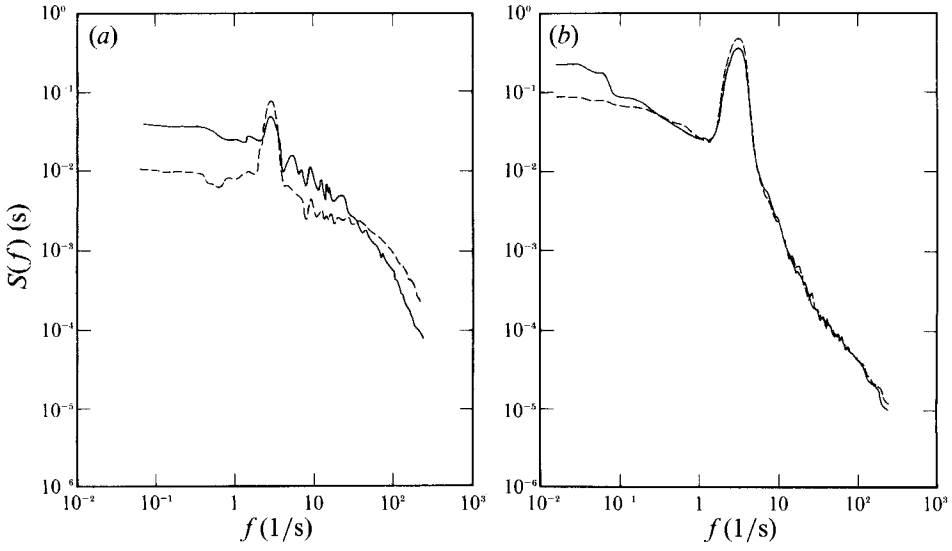


FIGURE 10. Profiles of power spectra of velocity fluctuations (*a*) in the air flow at $y = 0.018$ m and (*b*) in the water flow at $y = -0.015$ m for $U_\infty = 8.0$ m/s. The solid line shows the power spectrum of streamwise velocity fluctuation and the dashed line the power spectrum of vertical velocity fluctuation.

may affect the mass transfer across the air–water interface, and therefore we tried to estimate the frequency of appearance of the organized motions from the velocity signals measured in the air and water flows. Figure 10 shows typical profiles of the power spectra of the streamwise and vertical velocity fluctuations in each flow. Each spectrum shows a clear peak due to wave motions at the same frequency and the peak is especially remarkable for the water flow. Therefore, the wave components with periodic low frequencies in the velocity signals were eliminated by means of a digital bandpass filter (Bendat & Piersol 1971), and only the turbulence components were educed. Of course, the bandpass filtering may not be enough for estimating exactly quantities such as the energy distribution due to waves and turbulence, and it would be better to adopt a more sophisticated spectrum analysis. However, the present study aims to estimate only the appearance frequency of the organized motions exactly, which is obviously higher than that of the waves, as discussed later. For this purpose, the present filtering method was adequate for the velocity fluctuations, which have clear spectrum peaks at the lower frequency as in figure 10.

Figure 11 (*a*, *b*) shows typical time records of the filtered streamwise and vertical velocity fluctuations and Reynolds stress measured in the air and water flows. Here it should be noted that the velocities are not simultaneously measured for both air and water flows. It can be seen that negative peaks of the Reynolds stress intermittently appear in time records for both the air and water flows. When the negative peaks of the Reynolds stress appear, velocity signals ($u_G < 0, v_G > 0$, $u_G v_G < 0$ in the air flow and $u_L > 0, v_L < 0, u_L v_L < 0$ in the water flow) similar to typical bursting signals in the turbulent boundary layer are observed, as indicated by arrows in the figures. This, together with the flow visualization in figure 9, suggests that the organized motions appear in both the air and water flows. Kawamura & Toba (1988) have investigated the details of the turbulence structure in the air flow above the interface by means of both flow visualization and velocity measurements by a hot-wire anemometer moving with the wave, and they have also

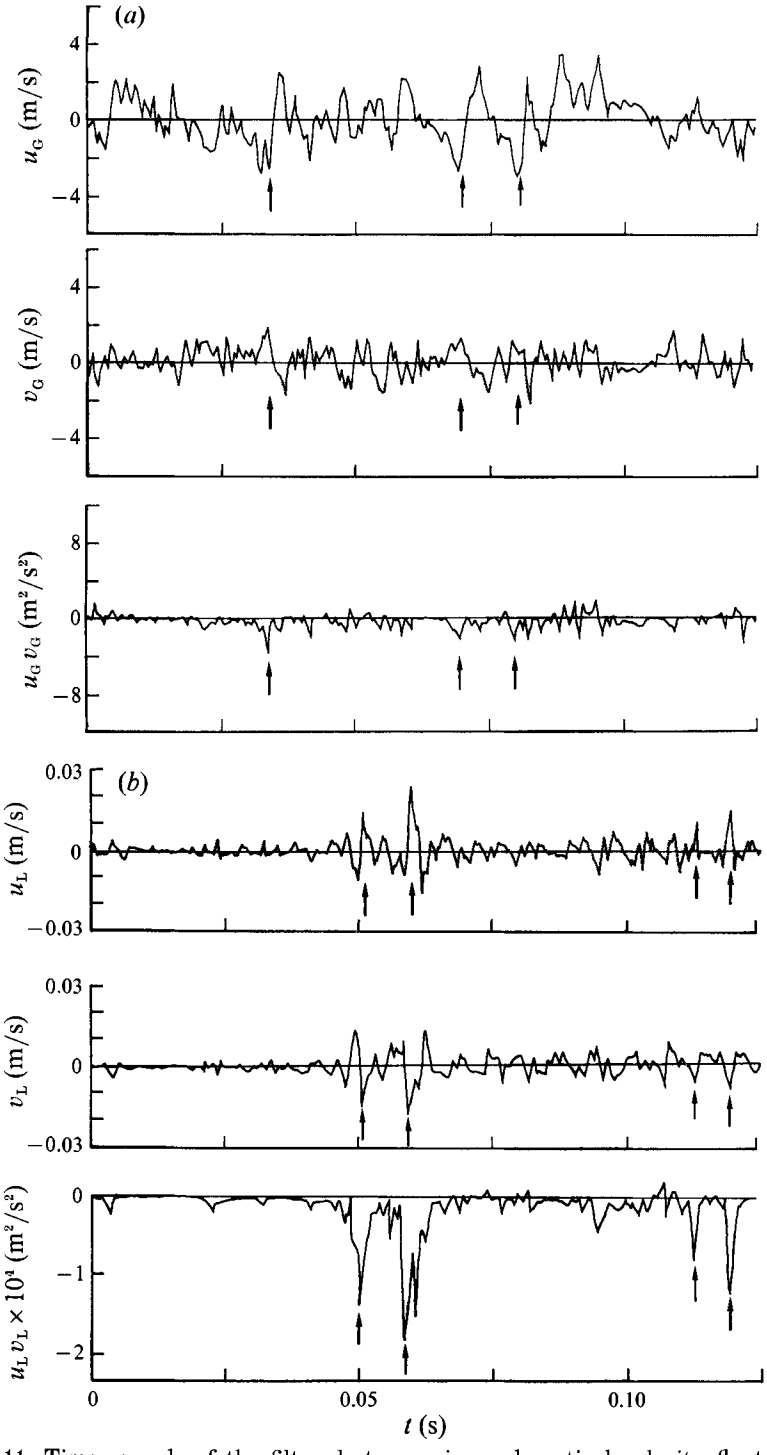


FIGURE 11. Time records of the filtered streamwise and vertical velocity fluctuations and the Reynolds stress (*a*) in the air flow at $y = 0.018$ m and (*b*) in the water flow at $y = -0.015$ m for $U_\infty = 8.0$ m/s. Arrows indicate the organized motions.

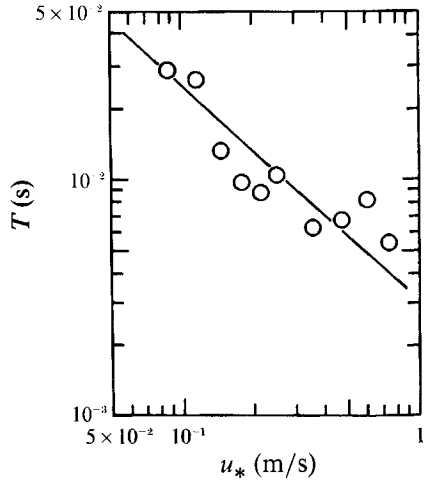


FIGURE 12. Correlation between the time duration of the organized motion and the friction velocity. The solid line shows (6).

confirmed that organized motion (which they call bursting motion) with velocity signals $u_G < 0$ and $v_G > 0$ and high Reynolds stress occur in the air boundary-layer flow. For water flow in a wind-wave tank, Cheung & Street (1988) have investigated the interaction between turbulence and waves by measuring instantaneous velocities below the interface, and they showed that strong turbulence is produced from the organized flow structures in the vicinity of the interface in the water flow.

To estimate the frequency of appearance of the above organized motion, the well-known VITA technique (Blackwelder & Kaplan 1976) was applied to the streamwise velocity signals in the air and water flows, $U_G$ and $U_L$. In the VITA technique, the variable-interval time average for a streamwise velocity $U(t)$ at a particular position is defined by

$$\hat{U}(t, T) = \frac{1}{T}\int_{t-\frac{1}{2}T}^{t+\frac{1}{2}T} U(s)\,\mathrm{d}s, \tag{3}$$

where $T$ is the averaging time. A localized measure of the velocity intensity is represented by the local variance

$$\widehat{\mathrm{var}}\,(t, T) = \widehat{U^2}(t, T) - [\hat{U}(t, T)]^2. \tag{4}$$

Using this variance, a detection function of the organized motion is defined by

$$D_V(t) = \begin{cases} 1 & \text{if } \widehat{\mathrm{var}}\,(t, T) > ku'^2 \\ 0 & \text{otherwise,} \end{cases} \tag{5}$$

where $k$ is the threshold level and $u'$ is the conventional r.m.s. of the streamwise velocity fluctuation $u(t)$. In addition, the number of intervals in which $D_V(t) = 1$ gives the number of appearances of the organized motion. Here the averaging time $T$ was determined by the averaged time duration of the organized motions shown in figure 12, and it was approximated by an empirical formula

$$T = 0.003u_*^{-0.92}. \tag{6}$$

The value of the threshold level $k$ was set to 0.16, where the profile of the number of appearances of the organized motions against the threshold level has a clear plateau. The details of the determination of the averaging time and threshold level are described in Komori *et al.* (1989).

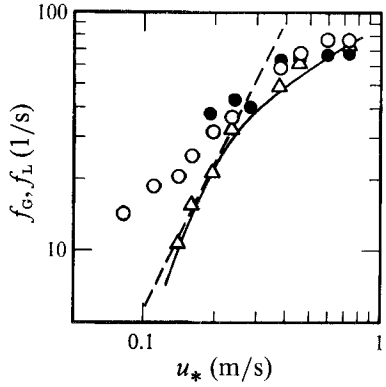


FIGURE 13. Variations of the frequencies of appearance of the organized motions with the friction velocity: ○, $f_G$ in the air flow; △, $f_L$ in the water flow; ●, $f_G$ estimated by flow visualization in the air flow. The solid line shows the frequency of appearance of the strong organized motions detected by the *uv*-quadrant method in the air flow, $f_{GS}$. The dashed line shows proportionality between $f_L$ and $u_*^2$.

Figure 13 shows the frequencies of the appearance of organized motions in the air and water flows, $f_G$ and $f_L$, versus the friction velocity $u_*$ on the air side. Both frequencies increase with increasing $u_*$, and in the high-shear region $u_* > 0.25$ m/s, $f_G$ is in good agreement with $f_L$. However, in the low-shear region $u_* < 0.25$ m/s, the frequencies deviate from each other, and $f_G$ becomes larger than $f_L$. That is, the organized motions appear more frequently in the air flow than in the water flow. This suggests that only strong organized motions with high turbulent shear in the air flow can induce the organized motions in the water flow. When considering the turbulence generation mechanism in a wind-wave tank (see figure 9), we can easily accept this assumption. Therefore, to educe strong organized motions with large momentum in the air flow, the *uv*-quadrant method (see Alfredsson & Johansson 1984) was used here.

In the *uv*-quadrant method, an event is considered to occur when the $u_G v_G$-signal exceeds a chosen threshold, i.e. when $|u_G v_G| > H$. Then, the detection function $D_Q(t)$ is defined by

$$D_Q(t) = \begin{cases} 1 & \text{if } |u_G v_G| > H \\ 0 & \text{otherwise,} \end{cases} \tag{7}$$

and the number of appearances of strong organized motions is given by the number of intervals in which $D_Q(t) = 1$. Here the negative peaks of the Reynolds stress in the second quadrant ($u_G < 0, v_G > 0$) were triggered by the threshold level $H$, since the frequency of appearance of such peaks in the second quadrant is about the same as for events detected with the VITA technique (Alfredsson & Johansson 1984). The value of the threshold level $H$ was found to give the same frequency as the value of $f_G$ detected by the VITA technique at $u_* = 0.25$ m/s, where $f_G$ and $f_L$ begin to deviate from each other. The value of $H$ was 0.2 m$^2$/s$^2$, and it corresponded to the minimum value of the Reynolds stress of the strong organized motions in the air flow, which can induce the organized motions in the water flow. The frequency of appearance of the strong organized motions, $f_{GS}$, is shown in figure 13 by the solid line. The frequency $f_{GS}$ is in good agreement with the frequency of organized motions on the water side over the whole range of $u_*$. This supports the assumption that only strong organized motions with large Reynolds stress in the air flow can induce organized motions in the water flow.

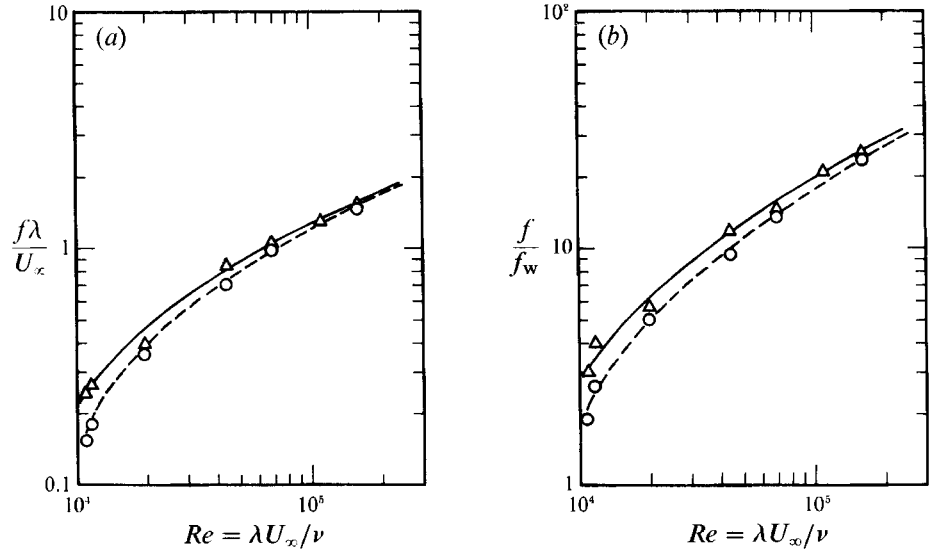


FIGURE 14. (*a*) Normalized frequencies of the organized motions versus the Reynolds number: ○, $f_L\lambda/U_\infty$ in the air flow; △, $f_G\lambda/U_\infty$ in the water flow. (*b*) The ratio of the frequency of the organized motion to the wave frequency versus the Reynolds number: ○, $f_L/f_W$; △, $f_G/f_W$.

To show that the organized motions in the air flow, visualized as in figure 9, correspond to the organized motions detected by the above VITA technique, the number of appearances of the smoke bulges observed in the air flow was counted by eye as objectively as possible, playing each frame of the high-speed video pictures. The frequency of organized motions counted from the flow visualization in the air flow is shown by solid circles in figure 13, and it well agrees with the frequency detected by the VITA technique, $f_G$. This suggests that the visualized organized motion in the air flow is well detected by the present VITA technique.

It should be noted that $f_L$ and $f_{GS}$ increase in proportion to the square of $u_*$ in the weakly sheared region $u_* < 0.25$ m/s as shown by a dashed line in figure 13, and the rate of increase decreases in the highly sheared region $u_* > 0.25$ m/s. The proportionality in the weakly sheared region is in good agreement with the results of Rashidi & Banerjee (1990) and Rashidi, Hetsroni & Banerjee (1991) in an open-channel flow with a non-wavy sheared interface. This suggests that in the weakly sheared region with small waves the main mechanism of turbulence production is similar to the bursting phenomena found by Rashidi & Banerjee (1990), but in the highly sheared region with bigger waves the turbulence is generated by the waves as shown in figure 9. Therefore, the frequencies of the organized motions are not simple functions of $u_*$. The decrease of the rate of increase of frequencies in the high-shear region may be attributed to the increased energy due to the speedup of the wind being mainly consumed by wave growth, and the energy transferring from the air flow to the water-side turbulence tends to saturate.

For reference, the frequencies of the organized motions, normalized by the wavelength $\lambda$ and free-stream velocity $U_\infty$, are plotted in figure 14(*a*) against the Reynolds number based on the wavelength and the viscosity of the air. A behaviour similar to $f_G$ and $f_L$ in figure 13 is found. The frequencies normalized by the wave frequency $f_W$ are also plotted in figure 14(*b*) against the Reynolds number. The frequencies of the organized motions are much larger than the wave frequency, which means that on average some of the organized motions intermittently occur above a

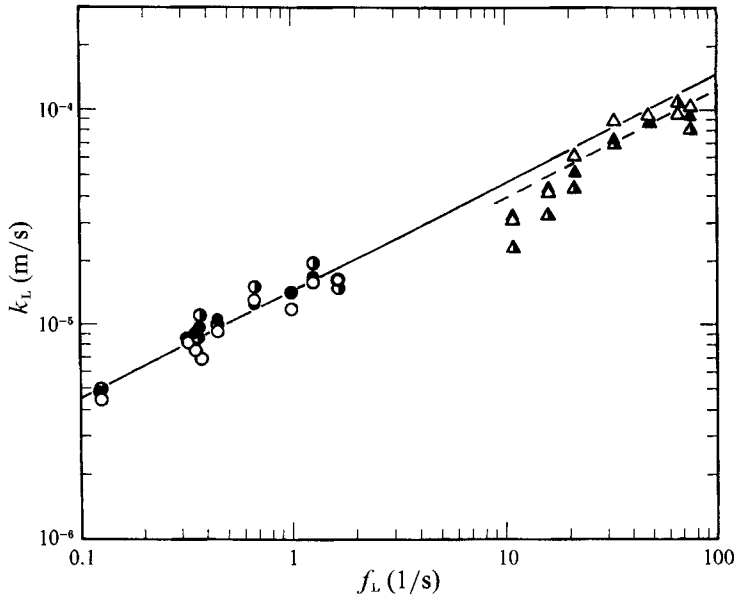


FIGURE 15. Correlation between the frequency of appearance of the organized motion in the water flow and mass transfer velocity: △, measurements in the present wind-wave tank with the sheared interface; ○, measurements in an open-channel flow with the unsheared interface (Komori *et al.* 1989); ▲ and ●, predictions by the surface-renewal model using (15); ◮ and ◑, predictions by the surface-renewal model using (16). The solid line shows (8) and the dashed line shows $k_L = 0.29(D_L f_L)^{\frac{1}{2}}$.

wave. In particular, the value of $f_L/f_W$ at the maximum Reynolds number suggests that the surface-renewal motion has the scale of about one-twentieth that of the wave, as shown by the sketch in figure 9.

### 3.3. *Relationship between mass transfer and turbulence structure*

Komori *et al.* (1989, 1990) and Komori (1991) have showed that the organized motions appearing in the interfacial region on the liquid side renew the interface and control the mass transfer in open-channel flows with zero-shear interfaces. Their experiments on the absorption for $CO_2$ and Ar gases also showed that the relation between the mass transfer velocity $k_L$ and surface-renewal frequency $f_L$ on the liquid side is approximated by

$$k_L = 0.34(D_L f_L)^{\frac{1}{2}}, \tag{8}$$

where $D_L$ is the molecular diffusivity of gas on the liquid side. The constant of 0.34 will be discussed later through a surface-renewal model. When the organized motion induced on the water side renews the sheared interface in the present wind-wave tank, it will also control the mass transfer. To compare the present mass transfer velocity with that for the unsheared interface, the mass transfer velocity $k_L$ in figure 8(*a*) is replotted in figure 15 with the measurements for the unsheared interface of Komori *et al.* (1989, 1990) against the frequency of appearance of the surface-renewal motions induced in the water flow, $f_L$. The measurements of $k_L$ for the sheared interface are approximately proportional to the root of $f_L$, and they show the values close to (8) obtained for the unsheared interface (though the measurements are better approximated by $k_L = 0.29(D_L f_L)^{\frac{1}{2}}$ as indicated by a dashed line in the figure). Here it should be noted that the present mass transfer measurements for the sheared interface were done only for $CO_2$. Therefore the proportionality between $k_L$ and $D_L^{\frac{1}{2}}$

was not experimentally conformed for the sheared interface. However, as shown below, the measurements of Komori (1991) for unsheared interfaces of $CO_2$–water and Ar–water show the same proportionality when the surface-renewal concept is appropriate.

It is now interesting to discuss why $k_L$ in two different flows – with sheared and unsheared interfaces – is roughly approximated by the same relation (8). Inherently, (8) suggests that the surface-renewal concept is appropriate. According to an original surface-renewal model of Higbie (1935), the coefficient of (8) should, however, be equal to unity, whereas the present value of 0.34 is much smaller. Banerjee (1991) suspected that this difference may be attributed to surface contamination or an error in counting $f_L$ by Komori *et al.* (1989, 1990) and Komori (1991), and he has developed a modified surface-renewal model based on the idea of turbulent patches in which the ratio of the turbulent patches to the total area is determined by experiments. On the other hand, Asher & Pankow (1991) have insisted that the surface-renewal model is appropriate for calculating $k_L$ only at a vacuum-cleaned interface by comparing their measurements with the Higbie's model, and they suggested that the surface-renewal model may not be applicable to mass transfer across air–water interfaces in nature. However, it is ambiguous to discuss the validity of the surface-renewal concept only by comparing the measurements of $k_L$ with 'the Higbie model' as in Asher & Pankow (1991), since the Higbie's model is a crude one-dimensional model which cannot inherently describe convective surface-renewal motion. Further, Asher & Pankow measured the surface-renewal frequency by an uncertain conditionally averaging technique, and they have not compared $k_L$ for both clean and contaminated gas–liquid interfaces with more reliable frequencies such as an oscillating frequency of the turbulence grid. In practice, the surface-renewal motion is far from the ideal motion assumed in the Higbie's model, and it is the vortical organized motion that intermittently appears at the gas–liquid interface. Thus, Fortescue & Pearson (1967) improved the crude Higbie model and proposed a two-dimensional eddy-cell model which an eddy cell periodically and continuously renews the free surface. However, their model does not include the time fraction of the surface renewal. That is, the surface-renewal organized motion does not continue to renew the free surface during the whole time, but only for a period. Therefore, we tried to add the effect of the time fraction to the eddy-cell model of Fortescue & Pearson (1967).

According to the model of Fortescue & Pearson (1967), the velocity components of an eddy-cell are given by

$$u = V \sin(\pi x/\Lambda) \cos(\pi y/\Lambda), \quad v = -V \cos(\pi x/\Lambda) \sin(\pi y/\Lambda), \tag{9}$$

where $V$ and $\Lambda$ are the velocity and length scales of an eddy cell, respectively, and the coordinate system of an eddy cell is shown in figure 16.

The steady mass transfer equation is given by

$$u(\partial C/\partial x) + v(\partial C/\partial y) = D_L(\partial^2 C/\partial x^2 + \partial^2 C/\partial y^2), \tag{10}$$

where $C$ is the normalized concentration and $D_L$ is the molecular diffusivity of gas on the liquid side. The boundary conditions in figure 16 are given by

$$C = 1 \quad \text{at} \quad y = 0, \quad C = 0 \quad \text{at} \quad y = \Lambda, \quad \partial C/\partial x = 0 \quad \text{at} \quad x = 0 \quad \text{and} \quad x = \Lambda. \tag{11}$$

We numerically solved (10) by using a finite difference method with $100 \times 100$ grid points, and we computed the mass transfer coefficient $k_L$ from the concentration gradient at the free surface. The Péclet number, $Pe = V\Lambda/D_L$, was kept at 100,

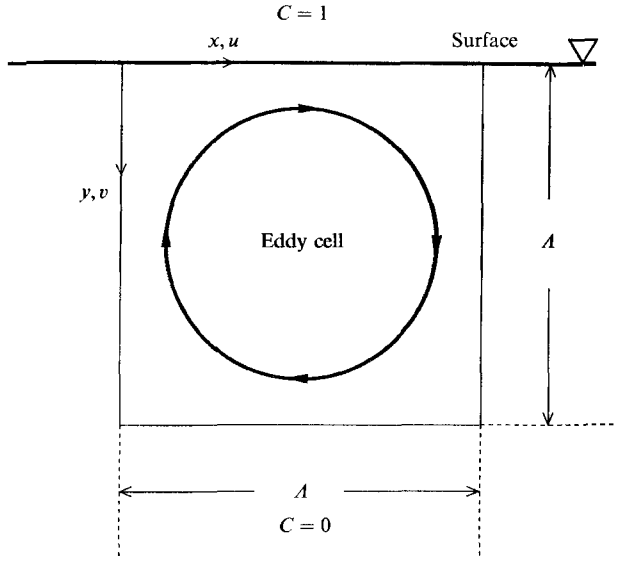


FIGURE 16. Sketch of an eddy-cell model.

because $k_L$ was almost independent of it for Péclet number larger than about 10. The computed $k_L$ was a function of the root of the product of the ratio of the velocity scale to length scale ($V/\Lambda$) and molecular diffusivity ($D_L$) for a Péclet number greater than 10 and it was given by

$$k_L = 0.9(D_L V/\Lambda)^{\frac{1}{2}}. \tag{12}$$

The relation (12) is in good agreement with the calculation of Luk & Lee (1986).

To consider the fraction of time that the surface renewal occurs, we assume that surface renewal occurs for the time of appearance of the organized motion at the free surface and otherwise it stops. The time duration (presence time) of the surface renewal, $T$, is given by an empirical correlation of (6) for the present sheared interface and by the empirical formula $45\nu/u_*^2$ for the unsheared interface in an open-channel flow of Komori *et al.* (1989). Then, the time fraction, $t^*$, is defined by the ratio of the total time duration (presence time) of the surface renewal to the total measurement time:

$$t^* = Tf_L, \tag{13}$$

and $k_L$ is given by

$$k_L = 0.9t^*(D_L V/\Lambda)^{\frac{1}{2}}. \tag{14}$$

The idea of the time fraction may describe more realistically the effect of the surface-renewal motion than continuous surface renewal, and it may be close to the concept of turbulent patches of Banerjee (1991).

The problem is how to determine $V/\Lambda$ in (14). Here, we tried two estimation methods. The first assumes that $V/\Lambda$ is proportional to the reciprocal of the time duration of the surface renewal at the free surface:

$$V/\Lambda = \sigma/T, \tag{15}$$

where $\sigma$ is a constant. When the surface-renewal eddy rotates fully once at the free surface during a duration $T$, $\sigma$ is equal to unity. However, in practical turbulent flows, $\sigma$ may not be always equal to unity, and it should be estimated by experiments. Unfortunately, it is so difficult to measure $\sigma$ that we determined the value of $\sigma = 0.4$ by comparing the measurements of $k_L$ as a parameter. The second method uses the assumption that

$$V/\Lambda = f_L. \tag{16}$$

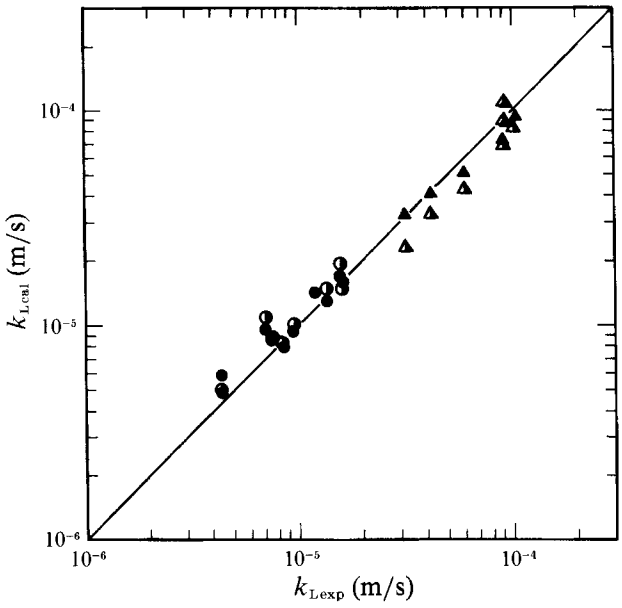


FIGURE 17. Comparison between the predicted and measured $k_L$: ▲, ●, comparisons between the predictions by the surface-renewal model using (15) and the measurements both in the present wind-wave tank with the sheared interface and in an open-channel flow with the unsheared interface (Komori *et al.* 1989), respectively; ◭, ◑, comparisons between the predictions by the surface-renewal model using (16) and the measurements both in the present wind-wave tank with the sheared interface and in an open-channel flow with the unsheared interface (Komori *et al.* 1989), respectively.

Equation (16) means that a surface-renewal eddy is successively generated at frequency $f_L$ in the bulk flow and it appears at the free surface during the time duration $T$.

Figure 17 shows comparisons between the model predictions of $k_L$ and the measurements for both sheared and unsheared interfaces. Predictions using both (15) and (16) agree comparatively well with the measurements both in the present wind-wave tank with the sheared interface and in the open-channel flow of Komori *et al.* (1989) with the unsheared interface, and the agreement with the surface-renewal model based on (15) is especially remarkable. The results suggest that the surface-renewal concept is appropriate for both unsheared and sheared interfaces. The predictions can also suggest why $k_L$ is approximated by (8). Predictions of $k_L$ using both (15) and (16) are again shown in figure 15, together with the measurements. The predictions explain well the behaviour of $k_L$ against $f_L$. The results also show that strictly $k_L$ deviates from (8) for the sheared interface and so it is only an approximation.

The above results show that the mass transfer is controlled by the liquid-side surface-renewal motion appearing at the gas–liquid interface and it can be estimated by the surface-renewal eddy-cell model based on the time-fraction concept. The presence or absence of interfacial shear affects the values of the surface-renewal frequency and the time fraction of the surface renewal. Thus, in the present wind-wave tank, the surface-renewal motion is induced, through interfacial shear, in the water flow by the strong organized motion in the air flow, and the renewal motion controls the mass transfer across the sheared interface. The relation of $k_L$ to the friction velocity $u_*$ in figure 8(*a*) can also be explained by the surface-renewal

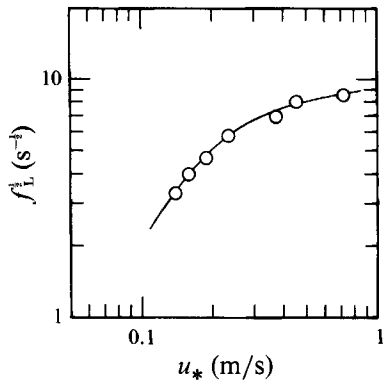


FIGURE 18. Variation of the root of the surface-renewal frequency with the friction velocity. The line shows the best fit curve.

concept of $k_L \propto f_L^{\frac{1}{2}}$, together with the relation between $f_L^{\frac{1}{2}}$ and $u_*$ shown in figure 18. That is, $f_L^{\frac{1}{2}}$ increases in the region $u_* < 0.25$ m/s, but its rate of increase decreases with increasing $u_*$ in the high-shear region $u_* > 0.25$ m/s. This behaviour of $f_L^{\frac{1}{2}}$ is quite similar to that of $k_L$ in figure 8(*a*). As discussed earlier, $f_L^{\frac{1}{2}}$ in the high-shear region suggests that the energy transferring from the air flow to the turbulence in the water flow may tend to saturate. For the extremely high shear region beyond the present measurements, the waves will be broken and the number of smaller-scale surface-renewal motions may rapidly increase with $u_*$. Also, many bubbles will be entrained into the water flow. Then, $k_L$ increases again, as shown by the jump in Merlivat & Mémery's (1983), Wanninkhof & Bliven's (1991) and our recent data. Though our experiments could not be carried out for extremely high shear because of the power limit of the wind fan, they suggest that the mass transfer velocity should not be assumed to increase proportionally with the wind shear. Furthermore, most published studies have tried to find the correlation between the mass transfer velocity and the friction velocity or wind speed, but this study warns that we should concentrate on estimating the frequency of appearance of the surface-renewal motions which occur just below the air–water interface in practical flows and the presence time of the surface-renewal motions. If we can estimate the frequency of the surface-renewal motions in the interfacial region in an arbitrary flow with an air–water interface and their presence time by using a direct numerical simulation or a sophisticated experimental technique, we will be able to easily estimate the $CO_2$ transfer velocity from (14), regardless of whether the interface is sheared or unsheared.

## 4. Conclusions

The mass transfer mechanism across a sheared air–water interface without bubble entrainment due to intense wave breaking was experimentally investigated in relation to the organized motion in the interfacial region in a wind-wave tank. The main results from this study can be summarized as follows.

(i) The mass transfer across a sheared air–water interface is intensively promoted by wind shear. However, the effect of the wind shear tends to saturate in the high-shear region, and there the rate of increase of the mass transfer velocity decreases rapidly. The effect of wind shear on the mass transfer velocity can be explained by introducing the surface-renewal concept, that is, the frequency of appearance of

surface-renewal motions on the water side. The mass transfer velocity is approximately correlated with the root of the frequency of appearance of the surface-renewal motions in the water flow. The surface-renewal frequency increases with increasing wind shear, but in the high-shear region the rate of increase tends to decrease. This results in the observed behaviour of the relation between the mass transfer velocity and the wind shear.

(ii) The organized motions in the air flow intermittently appear on the front of the wave crest and there they induce surface-renewal motions in the water flow through high shear stress on the interface. The surface-renewal motions control mass transfer across a wavy sheared gas–liquid interface.

(iii) The mass transfer velocity can be well estimated by the surface-renewal eddy-cell model based on the concept of the time fraction of the surface renewal both for the sheared interface in the present wind-wave tank and for the unsheared interface in an open-channel flow of Komori *et al.* (1989), when the surface-renewal frequency and the time duration of the surface renewal are measured.

The authors thank H. Kobayashi, Y. Inoue and Y. Yamashita for their great help in conducting experiments and numerical calculations, Professor J. C. R. Hunt of the UK Meteorological Office and the referees for useful discussion on the turbulence generation mechanism over the waves, and Professor Y. Toba of Tohoku University for his kind suggestion on how to construct a wind-wave tank. This work was supported by the Japanese Ministry of Education, Science and Culture through Grants-in-Aid (Nos. 02455016 and 04232218) and the Mitsubishi Foundation.

## REFERENCES

Alfredsson, P. H. & Johansson, A. V. 1984 On the detection of turbulence-generating events. *J. Fluid Mech.* **139**, 325–345.

Asher, W. E. & Pankow, J. F. 1991 Prediction of gas/water mass transport coefficient by a surface-renewal model. *Environ. Sci. Technol.* **25**, 1294–1300.

Banerjee, S. 1990 Turbulence structure and transport mechanism at interfaces. In *Proc. Ninth Intl Heat Transfer Conf.* (ed. G. Hetsroni), vol. 1, pp. 395–418. Hemisphere.

Banerjee, S. 1991 Turbulence/interface interactions. In *Phase-Interface Phenomena in Multiphase Flow* (ed. G. F. Hewitt, F. Mayinger & J. R. Riznic), pp. 3–19. Hemisphere.

Bendat, J. S. & Piersol, A. G. 1971 *RANDAM DATA: Analysis and Measurement Procedures.* John Wiley & Sons.

Blackwelder, R. F. & Kaplan, R. E. 1976 On the wall structure of the turbulent boundary layer. *J. Fluid Mech.* **76**, 89–112.

Broecker, W. S. & Peng, T. H. 1974 Gas exchange rates between air and sea. *Tellus* **26**, 21–35.

Broecker, H. C., Petermann, J. & Siems, W. 1978 The influence of wind on $CO_2$-exchange in a wind-wave tunnel, including the effects of monolayers. *J. Mar. Res.* **36**, 595–610.

Broecker, H. C. & Siems, W. 1984 The role of bubbles for gas transfer from water to air at higher wind speeds: experiments in the wind-wave facility in Hamburg. In *Gas Transfer at Water Surfaces* (ed. W. Brutsaert & G. H. Jirka), pp. 229–236. Reidel.

Cheung, T. K. & Street, R. L. 1988 The turbulent layer in the water at an air–water interface. *J. Fluid Mech.* **194**, 133–151.

Fortescue, G. E. & Pearson, J. R. A. 1967 On gas absorption into a turbulent liquid. *Chem. Engng Sci.* **22**, 1163–1176.

Hidy, G. M. & Plate, E. J. 1966 Wind action on water standing in a laboratory channel. *J. Fluid Mech.* **26**, 651–687.

Higbie, R. 1935 The rate of absorption of a pure gas into a still liquid during short periods of exposure. *Trans. AIChE* **31**, 365–388.

JÄHNE, B. 1980 Zur parametrisierung des gasaustausches mit hilfe von laborexperimenten. Dissertation, Institut fur Umweltphysik, University of Heidelberg.

JÄHNE, B., MUNNICH, K. O. & SIEGENTHALER, U. 1979 Measurements of gas exchange and momentum transfer in a circular wind-water tunnel. *Tellus* **31**, 321–329.

JIRKA, G. H. & BRUTSAERT, W. 1984 Measurements of wind effects on water-side controlled gas exchange in riverine systems. In *Gas Transfer at Water Surfaces* (ed. W. Brutsaert & G. H. Jirka), pp. 437–446. Reidel.

KAWAMURA, H. & TOBA, Y. 1988 Ordered motion in the turbulent boundary layer over wind waves. *J. Fluid Mech.* **197**, 105–138.

KOMORI, S. 1991 Surface-renewal motions and mass transfer across gas–liquid interfaces in open-channel flows. In *Phase-Interface Phenomena in Multiphase Flow* (ed. G. F. Hewitt, F. Mayinger & J. R. Riznic), pp. 31–40. Hemisphere.

KOMORI, S., MURAKAMI, Y. & UEDA, H. 1989 The relationship between surface-renewal and bursting motions in an open-channel flow. *J. Fluid Mech.* **203**, 103–123.

KOMORI, S., NAGAOSA, R. & MURAKAMI, Y. 1990 Mass transfer into a turbulent liquid across the zero-shear gas–liquid interface. *AIChE J.* **36**, 957–960.

KOMORI, S., NAGAOSA, R. & MURAKAMI, Y. 1993 Turbulence structure and scalar transfer across a sheared air–water interface in a wind-wave tunnel. In *Proc. 4th European Turbulence Conf.* (ed. F. T. M. Nieuwstadt). Kluwer (in press).

LAM, K. & BANERJEE, S. 1992 On the condition of streak formation in a bounded turbulent flow. *Phys. Fluids* A **4**, 306–320.

LISS, P. S. 1973 Processes of gas exchange across an air–water interface. *Deep-Sea Res.* **20**, 221–238.

LISS, P. S. & MERLIVAT, L. 1986 Air–sea gas exchange rates: introduction and synthesis. In *The Role of Air–Sea Exchange in Geochemical Cycling* (ed. P. Buat-Menard), pp. 113–127. Reidel.

LUK, S. & LEE, Y. H. 1986 Mass transfer in eddies close to air–water interface. *AIChE J.* **32**, 1546–1554.

MCCREADY, M. J. & HANRATTY, T. J. 1985 Effect of air shear on gas absorption by a liquid film. *AIChE J.* **31**, 2066–2074.

MÉMERY, L. & MERLIVAT, L. 1984 Contribution of bubbles to gas transfer across an air–water interface. In *Gas Transfer at Water Surfaces* (ed. W. Brutsaert & G. H. Jirka), pp. 247–253. Reidel.

MERLIVAT, L. & MÉMERY, L. 1983 Gas exchange across an air–water interface; experimental results and modeling of bubble contribution to transfer. *J. Geophys. Res.* **88**, 707–724.

PLANT, W. J. & WRIGHT, J. W. 1977 Growth and equilibrium of short gravity waves in a wind-wave tank. *J. Fluid Mech.* **82**, 767–793.

RASHIDI, M. & BANERJEE, S. 1990 The effect of boundary conditions and shear rate on streak formation and breakdown in turbulent channel flows. *Phys. Fluids* A **2**, 1827–1838.

RASHIDI, M., HETSRONI, G. & BANERJEE, S. 1991 Mechanisms of heat and mass transport at gas-liquid interfaces. *Intl J. Heat Mass Transfer* **34**, 1799–1810.

ROETHER, W. & KROMER, B. 1984 Optimum application of the radon deficit method to obtain air–sea gas exchange rates. In *Gas Transfer at Water Surfaces* (ed. W. Brutsaert & G. H. Jirka), pp. 447–457. Reidel.

SMETHIE, W., TAKAHASHI, T. & CHIPMAN, D. W. 1985 Gas exchange and $CO_2$ flux in the tropical atlantic ocean determined from $^{222}Rn$ and $pCO_2$ measurements. *J. Geophys. Res.* **90**, 7005–7022.

WANNINKHOF, R. H. & BLIVEN, L. F. 1991 Relationship between gas exchange, wind speed, and radar backscatter in a large wind-wave tank. *J. Geophys. Res.* **96**, 2785–2796.

WATSON, A. J., UPSTILL-GODDARD, R. C. & LISS, P. S. 1991 Air–sea gas exchange in rough and stormy seas measured by a dual-tracer technique. *Nature* **349**, 145–147.

YOSHIKAWA, I., KAWAMURA, H., OKUDA, K. & TOBA, Y. 1988 Turbulent structure in water under laboratory wind waves. *J. Oceanogr. Soc. Japan* **44**, 143–156.

ZILKER, D. P. & HANRATTY, T. J. 1979 Influence of the amplitude of a solid wave wall on a turbulent flow. Part 2. Separated flows. *J. Fluid Mech.* **90**, 257–271.